Journal of Sound and Vibration 330 (2011) 287–307

Contents lists available at ScienceDirect

Journal of Sound and Vibration

journal homepage: www.elsevier.com/locate/jsvi

An electro-mechanical impedance model of a cracked composite beam with adhesively bonded piezoelectric patches

Wei Yan [a,*], J.B. Cai [b], W.Q. Chen [c]

[a] Faculty of Architectural, Civil Engineering and Environment, Ningbo University, Ningbo 315211, PR China
[b] Department of Civil Engineering, Zhejiang University, Zijingang Campus, Hangzhou 310058, PR China
[c] Department of Engineering Mechanics, Zhejiang University, Yuquan Campus, Hangzhou 310027, PR China

ARTICLE INFO

Article history:
Received 16 April 2010
Received in revised form
1 August 2010
Accepted 8 August 2010
Handling Editor: L.G. Tham
Available online 1 September 2010

ABSTRACT

A model of a laminated composite beam including multiple non-propagating part-through surface cracks as well as installed PZT transducers is presented based on the method of reverberation-ray matrix (MRRM) in this paper. Toward determining the local flexibility characteristics induced by the individual cracks, the concept of the massless rotational spring is applied. A Timoshenko beam theory is then used to simulate the behavior of the composite beam with open cracks. As a result, transverse shear and rotatory inertia effects are included in the model. Only one-dimensional axial vibration of the PZT wafer is considered and the imperfect interfacial bonding between PZT patches and the host beam is further investigated based on a Kelvin-type viscoelastic model. Then, an accurate electro-mechanical impedance (EMI) model can be established for crack detection in laminated beams. In this model, the effects of various parameters such as the ply-angle, fibre volume fraction, crack depth and position on the EMI signatures are highlighted. Furthermore, comparison with existent numerical results is presented to validate the present analysis.

1. Introduction

Fibre reinforced composites are being used extensively in aerospace, mechanical and maritime applications due to their high strength to weight ratio and excellent corrosion resistance [1]. During the service lifetime, the composite structures will be subjected to various loads and exposed to corrosive environment that may cause initiation of structural defects such as impact-induced damages [2], hole-type damages [3], delaminations [4–7], cracks [8–11], etc. These tiny flaws can get significant and finally lead to the catastrophic failure of the structures as time progresses. Thus, new reliable and inexpensive methods should be found to identify structural defects such as cracks at a very early stage and provide some estimate of the extent or severity of the damages.

It is well known that cracks initiating in a structure result in a reduction of the local stiffness and hence alter the global dynamic structural behavior. Consequently, the dynamic properties of the cracked structures contain information about the severity and location of the damage. Under this consideration, dynamic analysis has been explored for detecting and monitoring cracks occurring in composite materials for many years. Krawczuk and Ostachowicz [8] investigated the eigenfrequencies of a cantilever beam, made from graphite fibre reinforced polyimide, with a transverse open crack, which is modeled by a massless spring and the cracked beam finite element, respectively. Krawczuk et al. [9] presented a model

* Corresponding author. Tel.: +86 574 87609513; fax: +86 574 87600355.
E-mail address: yanwei4467@sohu.com (W. Yan).

0022-460X/$ - see front matter © 2010 Elsevier Ltd. All rights reserved.
doi:10.1016/j.jsv.2010.08.013

and an algorithm for creation of the characteristic matrices of a composite beam with a single transverse fatigue crack. Song et al. [10] analyzed the free bending vibration of cantilevered composite beam with multiple surface cracks by an exact solution methodology based on Laplace transform technique. Kisa [11] studied the effects of cracks on the dynamics of a cantilever composite beam using the finite element and the component mode synthesis methods. All of these investigations focus on dynamic properties of cracked composite beams at low frequencies and only the first few low-frequency modes are considered which are not sensitive enough to detect tiny yet potentially damaging cracks in the structure [12].

In the past decade, there have been extensive investigations on the electro-mechanical impedance (EMI) approach using piezoelectric sensors/actuators integrated onto structures to monitor their conditions [6,13–18]. The EMI signatures extracted from PZT wafers in the high-frequency range are directly related to the mechanical impedance of the bonded structure and thus are highly sensitive to minor changes in structural integrity. In the conventional EMI method, a pin force model is always assumed to simulate ideal bonding between PZT wafers and the host structure in which all the load transfer takes place over an infinitesimal region at the ends of the piezoelectric patches [19]. Recently, much attention has been paid on the effect of adhesive on the performance of piezoelectric elements [19–23], and connection between PZT patches and host structure is considered to be achieved through interfacial shear stress based on the shear lag model [20,23], see the paper of Crawley and Lius [24]. More recently, Han et al. [25] provided a comprehensive theoretical study of the effect of bonding layer, which is simulated by a Kelvin-type viscoelastic model, on the coupled electro-mechanical characteristics of a piezoelectric sensor bonded to an isotropic elastic substrate in the high-frequency range. In this interfacial viscoelastic model, a linear spring and a linear dashpot are parallel-connected [26,27]. However, the focus of their work was on the study of the effect of the material and geometric properties of the sensor and the bonding layer on the load transfer from the host medium to the sensor. No further information about the host structure, such as the crack depths and locations etc., was revealed in the high-frequency range.

In order to establish an accurate EMI model for crack detection in composite beams, another important issue, which relates to high-frequency dynamic analysis for a composite beam, should be considered carefully. The classical dynamic analysis techniques such as the finite element method (FEM) [8–11] and the transfer matrix method (TMM) [6] have been employed to investigate damaged composite beams. However, FEM is usually subjected to an inherent disadvantage because high-frequency analysis of structure inevitably involves a huge number of degrees of freedom, which result from the huge numbers of finite elements and nodes, for predicting sufficiently accurate frequencies. The transfer matrix method (TMM) is very powerful to analyze a regular structure consisting of many members because the number of resultant simultaneous equations can be greatly reduced. However, significant numerical difficulty at high frequency limits its application if the computation is completely executed on a computer [28]. Note that the method of reverberation-ray matrix (MRRM) [29,30], which is based on the concept of elastic wave propagation, has shown its great superiority on high-frequency dynamic analysis in our previous works [23,31]. The specific advantage of MRRM over the finite element method (FEM) and the transfer matrix method (TMM) has been well discussed in detail [29,31,32] and hence omitted here.

The main aim of this paper is to establish an accurate EMI model for analytical crack detection of a composite beam. The analysis is based on a Timoshenko beam model and the crack is treated as a massless rotational spring [8,10,11]. A pair of PZT patches with free ends symmetrically bonded onto the composite beam are assumed in a state of pure one-dimensional axial strain [13,20,23,25,31] under an out-of-phase harmonic electric force and hence a pure bending excitation is created [13]. Since the strain/stress transfer between PZT patches and the host beam is physically implemented through adhesives, a Kelvin-type viscoelastic law [25–27] is introduced into the EMI model for the first time to account for the bonding effect in order to improve signature sensitivity to cracks. Furthermore, the inertia effect of PZT actuator/sensor is taken into account because high-frequency electric field with typical propagation wave length comparable to the length of actuator is applied [25,33]. The method of reverberation-ray matrix (MRRM) is adopted to investigate the dynamics of the coupled smart structure system (piezoelectric patches-adhesive-cracked composite beam), which can overcome the difficulty associated with high-frequency analysis. Then, an analytical expression of impedance (or admittance) containing crack parameters as well as other physical parameters is derived for crack detection in the composite beams. Numerical results are finally obtained and discussed to demonstrate the validity of this analysis.

2. Formulations of composite beams with imperfectly bonded PZT patches

As shown in Fig. 1, a pair of PZT patches is bonded symmetrically onto the top and bottom surfaces of a cantilever composite beam and is driven by a fixed alternating electric field out of phase. To derive the governing equations, a beam segment bonded with PZT patches will be examined here as illustrated in Fig. 2. First, the equation of motion of PZT patch assumed in a state of 1D axial strain [25,31,33] is expressed as

$$E_p \frac{\partial^2 u_p}{\partial x^2} - \frac{\tau}{h_p} = \rho_p \frac{\partial^2 u_p}{\partial t^2}, \tag{1}$$

where u_p is the axial displacement of the PZT patches, ρ and E are the mass density and Young's modulus, respectively, h is the thickness (subscript p signifies the PZT patch), τ, varying along the bonding length, is the interfacial shear stress between the PZT patch (beam) and the adhesive, and t is the time variable. The shear stress τ distributed in the layer is

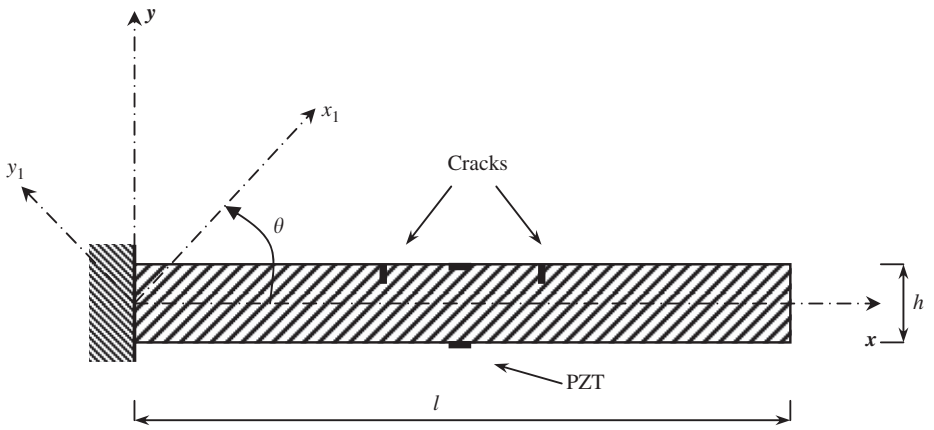

Fig. 1. Geometry of an intelligent beam with surface cracks.

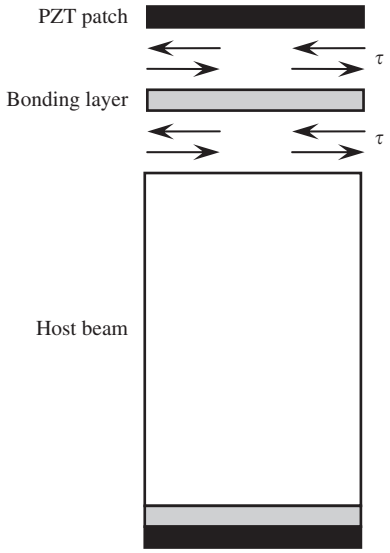

Fig. 2. A beam segment with adhesively bonded PZT patches.

determined by the following constitutive relation based on Kelvin-type viscoelastic model [25]:

$$\tau = \frac{G_b}{h_b}(u_p - u) + \frac{c_b}{h_b}\frac{\mathrm{d}(u_p - u)}{\mathrm{d}t}, \tag{2}$$

where G_b, h_b and c_b are the shear rigidity, the thickness and the coefficient of viscosity of the bonding layer, respectively, and

$$u = -\frac{h}{2}\frac{\partial w}{\partial x} \tag{3}$$

in which u and w are the axial displacement and transverse deflection of beam, respectively, and h is the thickness of the composite beam. It should be pointed out that the spring constant and the viscosity coefficient of the interface defined in Refs. [26,27] are respectively given by G_b/h_b and c_b/h_b here [25].

In this paper, it is assumed that the stress field of the cracked beam is influenced only in the region near to the crack according to the Saint Venant's principle and the discontinuity in the stiffness induced by the crack will be simulated by a massless rotational spring with infinitesimal length [8,10]. Thus, the composite beam is converted to a continuous-discrete model [10]. For the beam segment with piezoelectric elements, the governing equations are derived based on Timoshenko beam theory [10] as follows:

$$\begin{aligned} &\frac{\partial M}{\partial x} + \tau(x)bh - Q + \rho I\frac{\partial^2 \varphi}{\partial t^2} = 0, \quad M = -S_{11}I\frac{\partial \varphi}{\partial x} \\ &\frac{\partial Q}{\partial x} = \rho A\frac{\partial^2 w}{\partial t^2}, \quad Q = \kappa A S_{66}\left(\frac{\partial w}{\partial x} - \varphi\right) \end{aligned} \tag{4}$$

in which M and Q are the bending moment and shear force, I and A are the moment of area and cross sectional area, and κ is the shear correction factor, respectively. S_{11}, S_{66} and ρ denote the transverse bending stiffness, transverse shear stiffness and the mass density of the composite beam, respectively, and can be derived from the mechanical properties of the composite and the ply-angles of the fibre [8–11]. As a result, the transverse shear and rotatory inertia are included in this model. It is further assumed that the material of the composite beam is orthotropic, its principle axes x_10y_1 of orthotropy being rotated in the plane $x0y$ by an angle θ considered to be positive when it is measured from the positive x-axis in the counterclockwise direction as shown in Fig. 1. Then, on defining $m=\cos\theta$ and $n=\sin\theta$, we derive the following stiffness constants S_{ij} of the composite along the axes $x0y$ [11]:

$$\begin{aligned} S_{11} &= \bar{S}_{11}m^4+2(\bar{S}_{12}+2\bar{S}_{66})m^2n^2+\bar{S}_{22}n^4,\\ S_{66} &= \bar{S}_{66}m^4+(\bar{S}_{11}-2\bar{S}_{12}+\bar{S}_{22}-2\bar{S}_{66})m^2n^2+\bar{S}_{66}n^4, \end{aligned} \tag{5}$$

in which

$$\bar{S}_{11}=\frac{E_{11}}{1-\nu_{12}^2(E_{22}/E_{11})},\quad \bar{S}_{22}=\bar{S}_{11}\frac{E_{22}}{E_{11}},\quad \bar{S}_{12}=\nu_{12}\bar{S}_{22},\quad \bar{S}_{66}=G_{12}, \tag{6}$$

where the mechanical constants of the composite E_{11}, E_{22}, G_{12}, ν_{12} as well as the mass density ρ in Eq. (4) can be determined in Appendix A. Letting $u_p(x,t)=\overline{u}_p(x)e^{i\omega t}$, $u(x,t)=\overline{u}(x)e^{i\omega t}$, $w(x,t)=\overline{w}(x)e^{i\omega t}$, $\tau(x,t)=\overline{\tau}(x)e^{i\omega t}$ and $\varphi=\overline{\varphi}(x)e^{i\omega t}$ (ω is the angular frequency in rad/s, $i=\sqrt{-1}$ and $\omega=2\pi f$, f is the frequency in Hz) by the method of separation of variables yields the following differential equations from Eqs. (1) to (4):

$$\begin{aligned} &\frac{\partial\overline{\varphi}}{\partial x}=\frac{\partial^2\overline{w}}{\partial x^2}+\frac{\rho\omega^2}{\kappa S_{66}}\overline{w},\quad \overline{u}_p=c_1\frac{\partial^2\overline{\varphi}}{\partial x^2}+c_2\frac{\partial\overline{w}}{\partial x}+c_3\overline{\varphi},\\ &c_1=\frac{S_{11}h_bh^2}{12\eta_0G_b},\quad c_2=-\frac{h}{2}+\frac{\kappa S_{66}h_b}{\eta_0G_b},\quad c_3=\frac{\rho\omega^2h_bh^2-12\kappa S_{66}h_b}{12\eta_0G_b} \end{aligned} \tag{7}$$

and Eq. (2) can be rewritten as

$$\overline{\tau}=\frac{\eta_0G_b}{h_b}(\overline{u}_p-\overline{u}), \tag{8}$$

where

$$\eta_0=1+i\omega\frac{c_b}{G_b}. \tag{9}$$

Introduce the following parameter Γ and the stiffness ratio between beam and the piezoelectric patch:

$$\Gamma=\sqrt{(\overline{G}\theta_b/\overline{h}_b^2)(\psi+\alpha_0)/\psi},\quad \psi=S_{11}h/(E_ph_p), \tag{10}$$

where $\overline{G}=\eta_0G_b/E_p$, $\theta_b=h_b/h_p$, $\overline{h}_b=h_b/a$, ($a=l_p/2$, l_p is the length of PZT patch) and $\alpha_0=6$.

Setting $\eta_0=1$, i.e. $c_b=0$, we can get the classical shear lag model by Crawley and Lius [24], and the coefficient Γ becomes the well-known shear lag parameter [20,24,31]. For values of Γ greater than 30, the perfect bonding between the PZT patches and the host beam can be further assumed for engineering models [20,24]. Then, on defining $k_p^2=\rho_p\omega^2/E_p$, $k_s^2=\rho\omega^2/S_{11}$ and $k_G^2=\rho\omega^2/(\kappa S_{66})$, we derive the following six-order differential equation:

$$\frac{\partial^6\overline{w}}{\partial x^6}+A\frac{\partial^4\overline{w}}{\partial x^4}+B\frac{\partial^2\overline{w}}{\partial x^2}+C\overline{w}=0 \tag{11}$$

in which

$$\begin{aligned} A&=-(\Gamma/a)^2+k_p^2+k_s^2+k_G^2,\\ B&=(k_G^2k_s^2+k_G^2k_p^2+k_p^2k_s^2)-(k_G^2+k_s^2)\frac{\psi}{\psi+\alpha}(\Gamma/a)^2-k_p^2\frac{\alpha}{\psi+\alpha}(\Gamma/a)^2-\frac{12k_s^2}{h^2}\\ C&=\frac{12k_s^2}{h^2}\left[\frac{\psi}{\psi+\alpha}(\Gamma/a)^2-k_p^2\right]-k_G^2k_s^2\frac{\psi}{\psi+\alpha}(\Gamma/a)^2+k_G^2k_s^2k_p^2. \end{aligned} \tag{12}$$

Hence, the following relations can be obtained

$$\begin{aligned} w&=(a_1e^{\beta_1x}+a_2e^{\beta_2x}+a_3e^{\beta_3x}+d_1e^{-\beta_1x}+d_2e^{-\beta_2x}+d_3e^{-\beta_3x})e^{i\omega t},\\ \varphi&=(\gamma_1a_1e^{\beta_1x}+\gamma_2a_2e^{\beta_2x}+\gamma_3a_3e^{\beta_3x}-\gamma_1d_1e^{-\beta_1x}-\gamma_2d_2e^{-\beta_2x}-\gamma_3d_3e^{-\beta_3x})e^{i\omega t},\\ u_p&=(\lambda_1a_1e^{\beta_1x}+\lambda_2a_2e^{\beta_2x}+\lambda_3a_3e^{\beta_3x}-\lambda_1d_1e^{-\beta_1x}-\lambda_2d_2e^{-\beta_2x}-\lambda_3d_3e^{-\beta_3x})e^{i\omega t}, \end{aligned} \tag{13}$$

where $\gamma_i=\beta_i+k_G^2/\beta_i$, $\lambda_i=c_1\beta_i^2\gamma_i+c_2\beta_i+c_3\gamma_i$, ($i$=1,2,3), and a_i and d_i (i=1,2,3) are undetermined constants, and β_i are the characteristic roots of Eq. (11). For a general Timoshenko beam segment without bonding piezoelectric patches, the basic equation can readily be obtained by simply setting $\tau=0$ in Eq. (4) and the well-known homogeneous solution is

$$\begin{aligned} w(x,t)&=[a_1e^{k_1x}+a_2e^{k_2x}+d_1e^{-k_1x}+d_2e^{-k_2x}]e^{i\omega t},\\ \varphi(x,t)&=[\gamma_{s1}a_1e^{k_1x}+\gamma_{s2}a_2e^{k_2x}-\gamma_{s1}d_1e^{-k_1x}-\gamma_{s2}d_2e^{-k_2x}]e^{i\omega t} \end{aligned} \tag{14}$$

in which

$$k_1=\begin{cases}\sqrt{\dfrac{-\left(\dfrac{\omega^2}{\kappa c_s^2}+\dfrac{\omega^2}{c_0^2}\right)+\sqrt{\left(\dfrac{\omega^2}{\kappa c_s^2}-\dfrac{\omega^2}{c_0^2}\right)^2+\dfrac{4\omega^2}{c_0^2 r_s^2}}}{2}}, & \text{if } \omega<\sqrt{\kappa}c_s/r_s\\ \sqrt{\dfrac{\left(\dfrac{\omega^2}{\kappa c_s^2}+\dfrac{\omega^2}{c_0^2}\right)-\sqrt{\left(\dfrac{\omega^2}{\kappa c_s^2}-\dfrac{\omega^2}{c_0^2}\right)^2+\dfrac{4\omega^2}{c_0^2 r_s^2}}}{2}}\cdot \mathrm{i}, & \text{if } \omega>\sqrt{\kappa}c_s/r_s,\end{cases}$$

$$k_2=\sqrt{\frac{\left(\frac{\omega^2}{\kappa c_s^2}+\frac{\omega^2}{c_0^2}\right)+\sqrt{\left(\frac{\omega^2}{\kappa c_s^2}-\frac{\omega^2}{c_0^2}\right)^2+\frac{4\omega^2}{c_0^2 r_s^2}}}{2}}\cdot \mathrm{i}, \quad \gamma_{si}=k_i+\frac{\omega^2}{\kappa c_s^2 k_i}, \quad (i=1,2), \tag{15}$$

and $c_s=\sqrt{S_{66}/\rho}$, $c_0=\sqrt{S_{11}/\rho}$ and $r_s=\sqrt{I/A}=h/\sqrt{12}$.

It is well known that a surface crack on a structural member introduces a local flexibility that is a function of the crack depth, material elastic constants and the loading modes. With account taken of the fact that the slender composite beam is subjected only to the bending moment in this paper, fracture mode | is considered to be accurate enough to analyze the transverse open crack [8,10] and thus the non-dimensional flexibility is given as [8,10]:

$$\Theta=6D_1S_{11}\pi\frac{h}{l}\int_0^{\bar{c}}[\bar{c}Y_{\mathrm{I}}(\zeta)F_{\mathrm{IM}}^2(\bar{c})]\mathrm{d}\bar{c}, \tag{16}$$

where $\bar{c}=c/h$, c is the crack depth and

$$D_1=-0.5\bar{b}_{22}\mathrm{Im}\left(\frac{s_1+s_2}{s_1s_2}\right), \quad Y_{\mathrm{I}}(\zeta)=1+0.1(\zeta-1)-0.016(\zeta-1)^2+0.002(\zeta-1)^3,$$
$$\zeta=\frac{\sqrt{E_{11}E_{22}}}{2G_{12}}-\sqrt{\nu_{12}\nu_{21}}, \quad F_{\mathrm{IM}}(\bar{c})=\frac{\sqrt{\tan\gamma/\gamma}}{\cos\gamma}\left[0.923+0.199(1-\sin\gamma)^4\right], \quad \gamma=\frac{\pi\bar{c}}{2} \tag{17}$$

in which s_1 and s_2 are the characteristic roots of the following equation:

$$\bar{b}_{11}s^4-2\bar{b}_{16}s^3+(2\bar{b}_{12}+\bar{b}_{66})s^2-2\bar{b}_{26}s+\bar{b}_{22}=0. \tag{18}$$

All elastic constants E_{11}, E_{22}, G_{12}, ν_{12}, ν_{21} and $\bar{b}_{ij}$ in Eqs. (17) and (18) will be determined in Appendix A.

3. EMI model based on MRRM

For a composite beam with multiple cracks and bonded PZT patches, the whole composite beam should be divided into several successively connected beam segments with small and finite length and each beam element can thus be regarded as homogeneous. In MRRM, a major step is to set up two local coordinate systems for each beam segment, as shown in Fig. 3. It is assumed that the PZT patches are bonded onto *JK* segment and the fixed end and the free end of the composite beam are denoted as nodes 0 and *N*, respectively. If multiple cracks are located at joints 1, *I*, *L*, *M*, etc., the whole beam can then be separated into 0–1, 1–2, …, *I*–*J*, *J*–*K*, …, *L*–*M*, *M*–*N* with *N* beam segments and *N*+1 nodes. It should be noted that, for a uniform beam with homogenous material and geometric properties, we can treat the whole beam as one segment using the MRRM formulation. This is greatly different from FEM which requires a number of beam elements resulting in computationally expensive high-frequency analysis.

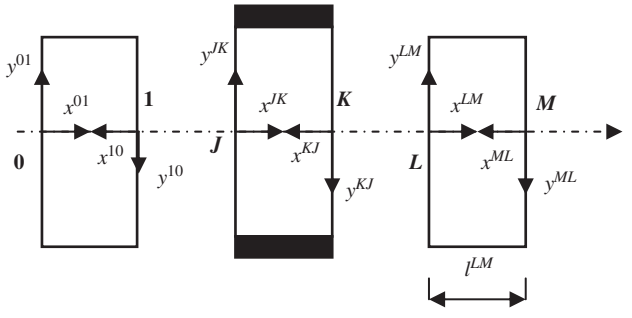

Fig. 3. The local coordinates for application of MRRM.

Having expressed beam deflection and rotation in Eqs. (13) and (14), the bending moment and shear force can be obtained according to Eq. (4). At the crack location such as joint L, we have

$$w^{LK}+w^{LM}=0,\quad M^{LK}+M^{LM}=0,\quad Q^{LK}=Q^{LM},\quad \varphi^{LM}-\varphi^{LK}=\Theta l\left(\frac{\partial\varphi}{\partial x}\right)^{LM}. \tag{19}$$

Here the non-dimensional flexibility Θ is determined by Eq. (16). The conditions given by Eq. (19) express the continuity of bending moments, shear forces and transverse displacements and the jump of the rotations at the crack location. Substituting the analytical expressions of bending moments, shear forces, transverse displacements and rotations into Eq. (19), the following relations in a matrix form are further obtained:

$$\mathbf{d}^L=\mathbf{S}^L\mathbf{a}^L, \tag{20}$$

where $\mathbf{d}^L=[d_1^{LK},\ d_2^{LK},\ d_1^{LM},\ d_2^{LM}]^{\mathrm{T}}$ is called the departing wave vector at joint L, and $\mathbf{a}^L=[a_1^{LK},a_2^{LK},a_1^{LM},a_2^{LM}]^{\mathrm{T}}$ is the arriving wave vector. The matrix $\mathbf{S}^L$ is called the local scattering matrix with rank four at joint L [29,30]. Eq. (20) establishes a scattering relation between various waves (traveling and standing waves) at node L.

At the left end of PZT patch at joint J, the following relations should be satisfied [24,31]:

$$\begin{gathered} w^{JI}+w^{JK}=0,\quad \varphi^{JI}=\varphi^{JK},\quad M^{JI}+M^{JK}=0,\quad Q^{JI}=Q^{JK},\quad \text{at}\quad x^{JI}=x^{JK}=0\\ \text{and}\quad \varepsilon_p=\frac{\partial u_p}{\partial x}=\frac{d_{31}V_3}{h_p}=\Lambda,\quad x^{JK}=0. \end{gathered} \tag{21}$$

where d_{31} and V_3 are the piezoelectric constant of PZT patch and the applied electric field, respectively. Then, we obtain

$$\mathbf{A}^J\mathbf{a}^J=\mathbf{B}^J\mathbf{d}^J+\mathbf{Q}_0, \tag{22}$$

The above equation can further be rewritten as follows:

$$\mathbf{d}^J=\mathbf{S}^J\mathbf{a}^J-(\mathbf{B}^J)^{-1}\mathbf{Q}_0,\quad \mathbf{S}^J=(\mathbf{B}^J)^{-1}\mathbf{A}^J,\quad \mathbf{Q}_0=\begin{bmatrix}0 & 0 & 0 & 0 & \Lambda\end{bmatrix}^{\mathrm{T}} \tag{23}$$

where $\mathbf{d}^J=[\,d_1^{JI}\ \ d_2^{JI}\ \ d_1^{JK}\ \ d_2^{JK}\ \ d_3^{JK}\,]^{\mathrm{T}}$ and $\mathbf{a}^J=[\,a_1^{JI}\ \ a_2^{JI}\ \ a_1^{JK}\ \ a_2^{JK}\ \ a_3^{JK}\,]^{\mathrm{T}}$ are the extended departing wave vector and arriving wave vector, respectively. The matrix $\mathbf{S}^J$ is the local scattering matrix of order 5×5 at joint J [29,30].

At the two ends (0 and N) of the composite beam, the boundary conditions instead of continuity conditions must be imposed. The scattering matrices at the two ends, $\mathbf{S}^0$ and $\mathbf{S}^N$, thus have a different form and the order is reduced to 2×2. For illustration, we consider the free end at $x=l$ (end N). To satisfy $Q=M=0$, the following relation can be obtained from Eqs. (4) and (14):

$$\begin{Bmatrix} d_1^{NM}\\ d_2^{NM}\end{Bmatrix}=\begin{bmatrix} \dfrac{\gamma_{s1}k_1(k_2-\gamma_{s2})+\gamma_{s2}k_2(k_1-\gamma_{s1})}{\gamma_{s2}k_2(k_1-\gamma_{s1})-\gamma_{s1}k_1(k_2-\gamma_{s2})} & \dfrac{2\gamma_{s2}k_2(k_2-\gamma_{s2})}{\gamma_{s2}k_2(k_1-\gamma_{s1})-\gamma_{s1}k_1(k_2-\gamma_{s2})}\\ \dfrac{2\gamma_{s1}k_1(k_1-\gamma_{s1})}{\gamma_{s1}k_1(k_2-\gamma_{s2})-\gamma_{s2}k_2(k_1-\gamma_{s1})} & \dfrac{\gamma_{s1}k_1(k_2-\gamma_{s2})+\gamma_{s2}k_2(k_1-\gamma_{s1})}{\gamma_{s1}k_1(k_2-\gamma_{s2})-\gamma_{s2}k_2(k_1-\gamma_{s1})}\end{bmatrix}\begin{Bmatrix} a_1^{NM}\\ a_2^{NM}\end{Bmatrix} \tag{24}$$

The above equation can be rewritten as $\mathbf{d}^N=\mathbf{S}^N\mathbf{a}^N$. Treatment of other boundary conditions is also similar. Combining all the local scattering matrices of $N-1$ joints and two ends, we arrive at a global scattering relation as follows:

$$\mathbf{d}=\mathrm{S}\mathrm{a}+\mathbf{Q} \tag{25}$$

where $\mathbf{d}=[(\mathbf{d}^0)^{\mathrm{T}},\ (\mathbf{d}^1)^{\mathrm{T}},\ldots,\ (\mathbf{d}^{N-1})^{\mathrm{T}},\ (\mathbf{d}^N)^{\mathrm{T}}]^{\mathrm{T}}$ is the global vector associated with departing waves, and $\mathbf{a}=[(\mathbf{a}^0)^{\mathrm{T}},\ (\mathbf{a}^1)^{\mathrm{T}},\ \ldots,\ (\mathbf{a}^{N-1})^{\mathrm{T}},\ (\mathbf{a}^N)^{\mathrm{T}}]^{\mathrm{T}}$ is the global vector associated with arriving waves [29,30]. The global scattering matrix $\mathbf{S}$ and the force vector $\mathbf{Q}$ are respectively obtained as

$$\begin{gathered} \mathbf{S}=\mathrm{diag}\begin{bmatrix}\mathbf{S}^0_{2\times2} & \mathbf{S}^1_{4\times4} & \cdots & \mathbf{S}^J_{5\times5} & \mathbf{S}^K_{5\times5} & \cdots & \mathbf{S}^M_{4\times4} & \mathbf{S}^N_{2\times2}\,\mathbf{S}\end{bmatrix},\\ \mathbf{Q}=\begin{bmatrix}(0_{2\times1})^{\mathrm{T}} & (0_{4\times1})^{\mathrm{T}} & \cdots & [-(\mathbf{B}^J)^{-1}\mathbf{Q}_0]^{\mathrm{T}} & [-(\mathbf{B}^K)^{-1}\mathbf{Q}_0]^{\mathrm{T}} & \cdots & (0_{4\times1})^{\mathrm{T}} & (0_{2\times1})^{\mathrm{T}}\end{bmatrix}^{\mathrm{T}}, \end{gathered} \tag{26}$$

where **diag**$[\cdot]$ signifies a diagonal matrix. There are totally $4N+2$ equations in Eq. (25) which are insufficient to determine the $8N+4$ unknowns of vectors $\mathbf{d}$ and $\mathbf{a}$. Hence, additional relations between these two vectors will be explored as follows.

For each member, two different local coordinate systems have been employed. With a unique physical reality, solutions of the two systems should predict identical result. More specifically, at identical point $x^{LM}=l^{LM}-x^{ML}$ on beam segment without bonded PZT patches, we should have

$$\overline{w}^{LM}(x^{LM})=-\overline{w}^{ML}(l^{LM}-x^{ML}), \tag{27}$$

which yields

$$\begin{aligned} a_1^{LM}e^{k_1^{LM}l^{LM}}&=-d_1^{ML},\quad a_2^{LM}e^{k_2^{LM}l^{LM}}=-d_2^{ML},\\ d_1^{LM}e^{-k_1^{LM}l^{LM}}&=-a_1^{ML},\quad d_2^{LM}e^{-k_2^{LM}l^{LM}}=-a_2^{ML}. \end{aligned} \tag{28}$$

For beam segment with bonded PZT patches, $x^{JK}=l^{JK}-x^{KJ}$, we also have

$$\overline{w}^{JK}(x^{JK})=-\overline{w}^{KJ}(l^{JK}-x^{JK}), \tag{29}$$

which gives

$$a_1^{JK} = -d_1^{KJ} e^{-\beta_1 l^{JK}}, \quad a_2^{JK} = -d_2^{KJ} e^{-\beta_2 l^{JK}}, \quad a_3^{JK} = -d_3^{KJ} e^{-\beta_3 l^{JK}},$$
$$d_1^{JK} = -a_1^{KJ} e^{\beta_1 l^{JK}}, \quad d_2^{JK} = -a_2^{KJ} e^{\beta_2 l^{JK}}, \quad d_3^{JK} = -a_3^{KJ} e^{\beta_3 l^{JK}}. \tag{30}$$

Eqs. (28) and (30) give the relations connecting the arriving waves in one local coordinates to the departing waves in another local coordinates, and are called phase relations [29,30]. New local vectors are introduced here: $\overline{\mathbf{d}}^L$ at joint L (not the end of PZT patch), and $\overline{\mathbf{d}}^J$ and $\overline{\mathbf{d}}^K$, respectively, at joint J and K (left end and right end of PZT patch) can be expressed as follows:

$$\overline{\mathbf{d}}^L = [d_1^{KL},\ d_2^{KL},\ d_1^{ML},\ d_2^{ML}]^T, \quad \overline{\mathbf{d}}^J = \begin{bmatrix} d_1^{IJ} & d_2^{IJ} & d_1^{KJ} & d_2^{KJ} & d_3^{KJ} \end{bmatrix}^{\mathrm{T}}$$
$$\overline{\mathbf{d}}^K = \begin{bmatrix} d_1^{JK} & d_2^{JK} & d_3^{JK} & d_1^{LK} & d_2^{LK} \end{bmatrix}^{\mathrm{T}}. \tag{31}$$

Hence, a new global vector $\overline{\mathbf{d}}$ for the departing waves is constructed as

$$\overline{\mathbf{d}} = [(\overline{\mathbf{d}}^0)^T,\ (\overline{\mathbf{d}}^1)^T,\ (\overline{\mathbf{d}}^2)^T, \ldots,\ (\overline{\mathbf{d}}^{N-}1)^T,\ (\overline{\mathbf{d}}^N)^T]^T, \tag{32}$$

where $\overline{\mathbf{d}}^0 = [d_1^{10},\ d_2^{10}]^T$ and $\overline{\mathbf{d}}^N = [d_1^{N-1,N},\ d_2^{N-1,N}]^T$. The global vectors $\overline{\mathbf{d}}$ and $\mathbf{d}$ contain the same elements but are sequenced in different orders. The two vectors thus can be related through a permutation matrix $\mathbf{U}$ as

$$\overline{\mathbf{d}} = \mathbf{U}\mathbf{d}, \tag{33}$$

Notice that Eqs. (28) and (30) are valid for both the beam segments without and with PZT patches. These relations can be combined in a matrix as follows:

$$\mathbf{a} = \mathbf{P}\overline{\mathbf{d}}, \tag{34}$$

where the total phase shift matrix $\mathbf{P}$ of order $(4N+2)\times(4N+2)$ is defined by

$$\mathbf{P} = \mathrm{diag}\begin{bmatrix} \mathbf{P}^{01} & \mathbf{P}^{12} & \cdots & \mathbf{P}^{JK} & \cdots & \mathbf{P}^{LM} & \mathbf{P}^{MN} \end{bmatrix}, \tag{35}$$

where $\mathbf{P}^{LM} = \mathrm{diag}[\ -e^{-k_1^{LM} l^{LM}} - e^{-k_2^{LM} l^{LM}} - e^{-k_1^{LM} l^{LM}} - e^{-k_2^{LM} l^{LM}}]$ for a beam segment without bonded PZT patches and meanwhile for a beam element with bonded PZT patches, we have $\mathbf{P}^{JK} = \mathrm{diag}[\ -\mathrm{e}^{-\beta_1 l^{JK}} - \mathrm{e}^{-\beta_2 l^{JK}} - \mathrm{e}^{-\beta_3 l^{JK}} - \mathrm{e}^{-\beta_1 l^{JK}} - \mathrm{e}^{-\beta_2 l^{JK}} - \mathrm{e}^{-\beta_3 l^{JK}}]$. Note that the phase matrices $\mathbf{P}^{ij}$ do not contain exponential functions with large positive indices and hence the numerical instability usually encountered in the conventional transfer matrix method (TMM) [28] can be avoided. This is a crucial point for the proper application of MRRM in high-frequency dynamic analysis of structures [23,31]. From Eqs. (25), (33) and (34), we have

$$\mathbf{d} = \mathbf{R}\mathbf{d} + \mathbf{Q}, \quad \mathbf{R} = \mathbf{S}\mathbf{P}\mathbf{U}, \tag{36}$$

where $\mathbf{R}$ is called the reverberation-ray matrix [29,30]. The following relations then hold:

$$\mathbf{d} = (\mathbf{I} - \mathbf{R})^{-1}\mathbf{Q}, \quad \mathbf{a} = \mathbf{P}\mathbf{U}\mathbf{d}. \tag{37}$$

Hence, all undetermined constants in Eqs. (13) and (14) can be solved from Eq. (37).

In this paper, the PZT patch is considered as a thin bar undergoing only axial motion. The corresponding constitutive equations are [13,20,23,31]

$$\varepsilon_p = \frac{T_1}{\overline{E}_p} + d_{31}E_3, \quad D_3 = \overline{\varepsilon}_{33}^T E_3 + d_{31}T_1, \tag{38}$$

where T_1 is the longitudinal stress, $\overline{\varepsilon}_{33}^T = \varepsilon_{33}^T(1-\delta \mathrm{i})$ is the complex dielectric constant, $\overline{E}_p = E_p(1+\eta i)$ is the complex Young's modulus, D_3 is the electric displacement, and η and δ are the mechanical and dielectric loss factors, respectively. From Eq. (38), we obtain

$$D_3 = (\overline{\varepsilon}_{33}^T - d_{31}^2\overline{E}_p)E_3 + d_{31}\overline{E}_p\varepsilon_p. \tag{39}$$

The electric current passing through PZT patch can be determined from the electric displacement as

$$I = \mathrm{i}\omega \iint D_3\, dxdy = i\omega w_p l_p(\overline{\varepsilon}_{33}^T - d_{31}^2\overline{E}_p)E_3 + \mathrm{i}\omega w_p d_{31}\overline{E}_p(u_p^R - u_p^L), \tag{40}$$

where w_p is the width of the PZT patch, u_p^R and u_p^L represent the axial displacements at the right and left sides of the PZT patch in the corresponding local coordinate, respectively. Since $E_3 = V_3/h_p$, the coupled electric admittance of the PZT patch

between two electrodes can be described by

$$Y=\frac{I}{V}=\frac{\mathrm{i}\omega w_p l_p(\bar{\varepsilon}_{33}^T-d_{31}^2\bar{E}_p)}{h_p}+\frac{\mathrm{i}\omega w_p d_{31}\bar{E}_p(u_p^R-u_p^L)}{V_3}. \tag{41}$$

From Eqs. (13), (21) and (37), we know that u_p is proportional to V_3. Without loss of generality, a unit voltage is assumed. Hence, Eq. (41) can be rewritten as

$$Y=\frac{\mathrm{i}\omega w_p l_p(\bar{\varepsilon}_{33}^T-d_{31}^2\bar{E}_p)}{h_p}+\mathrm{i}\omega w_p d_{31}\bar{E}_p(u_p^R-u_p^L). \tag{42}$$

The electric impedance Z can be expressed as the inverse of electric admittance. From Eq. (42), we can see that the first term on the right side is only related to the PZT patches, while the second term involves parameters of PZT patches, host beam and bond layer. In fact, the second term indicates the resonance condition of coupled PZT patch-bond layer-composite beam system in the frequency domain. We assume a pair of PZT patches is bonded to the *JK* beam segment as before. Substituting the expression for u_p in Eq. (13) into Eq. (42) and then using the phase relations again yields the electric admittance as

$$Y=\frac{\mathrm{i}\omega w_p l_p(\bar{\varepsilon}_{33}^T-d_{31}^2\bar{E}_p)}{h_p}+\mathrm{i}\omega w_p d_{31}\bar{E}_p\left(\sum_{j=1}^{3}\lambda_j(a_j^{KJ}-a_j^{JK}+d_j^{JK}-d_j^{KJ})\right). \tag{43}$$

Thus, from Eqs. (37) and (43), we can calculate the electric admittance (or electric impedance) of the PZT patch easily.

4. Numerical computations

4.1. Validation of the present model

To validate the present EMI model, numerical results are compared with available theoretical predications via the other methods. First, a cantilever beam with length 0.8 m and square cross-section 0.02×0.02 m^2 is assumed. A single crack of depth 2 mm is located at 0.12 m from the fixed end. The material properties of the beam corresponds to an isotropic material of Young's modulus $E=2.10\times10^{11}N/m^2$, Poisson's ratio v=0.35 and mass density ρ=7800 kg/m^3 [10]. The PZT patches are bonded symmetrically onto the cracked beam and are located at 0.3 m from the fixed end. All geometric parameters and material constants of the PZT patch are listed in Table 1. The lowest three natural frequencies are directly extracted from the EMI signatures using the present model (see Fig. 4) and they are listed in Table 2. Good agreement with published results [10,34] can be observed. Another single simply supported beam of square cross-section with width 12.7 mm, height 12.7 mm and length 400 mm is also considered for the comparison study. A single-sided open crack with depth 5 mm is located at 120 mm from the left end while the material properties of the host beam are [35]: Young's modulus $2.07\times10^{11}N/m^2$, density 7860 kg/m^3 and Poisson's ratio 0.3. From Fig. 5, the three natural frequencies extracted from the EM signatures are about 700, 1630 and 2830 Hz. These values differ slightly from the experiment results (700, 1616 and 2864 Hz) by an impact test [35] with the maximum error being less than 1.2%. Unless otherwise stated, perfect interfacial bonding is always assumed in this paper by taking c_b=0 and a large value of shear lag parameter Γ=43.7.

Then, a cantilever beam made of unidirectional graphite fibre-reinforced polyamide is always considered in the following investigation. The material properties of the composite, in terms of fibre and matrix, identified by the subscript f and m, respectively, are listed in Table 3 [8–11]. The geometrical characteristics, the length, height and width of the beam are further chosen as 1, 0.025 and 0.05 m, respectively [8,10]. The case considered in Ref. [10] will be adopted here for comparison study and it is associated with three cracks of an identical depth 5 mm located at different positions. The volume fraction of fibres V and the angle of the fibre θ are assumed to be 0.5 and 0°, respectively, and a pair of PZT patches symmetrically bonded onto the beam is located at 0.15 m from the fixed end. The first three natural frequencies can then be directly extracted from the conductance curves plotted in Fig. 6. The results of comparison are summarized in Table 4. We can see that the difference between the numerical results obtained by the present method and the calculated ones in Ref. [10] are less than 5% except for the first natural frequency for case A. Through further observations, we can find almost all corresponding natural frequencies obtained by the present method are higher than those calculated in Ref. [10]. This indicates that the resonant frequencies increase for a coupled PZT patch-bonding layer-host beam system considered here due to the well-known piezoelectric stiffening effect. It is similar to what is observed in Ref. [36] for an isotropic beam. In Fig. 6 and Table 4, three cases relating to the different crack locations are considered and are labeled as A(0.1; 0.2; 0.3), B(0.4; 0.5; 0.6) and C(0.7; 0.8; 0.9), respectively. The data in the brackets mean the distances between the crack position

Table 1
Material constants and geometric parameters of PZT patch.

Geometry (mm^3)	E_p (N/m^2)	η	ρ_p (kg/m^3)	d_{31} (m/V)	ε_{33}^T (F/m)	δ
$10\times10\times0.2$	6.67×10^{10}	0.03	7800	-2.10×10^{-10}	2.14×10^{-8}	0.0185

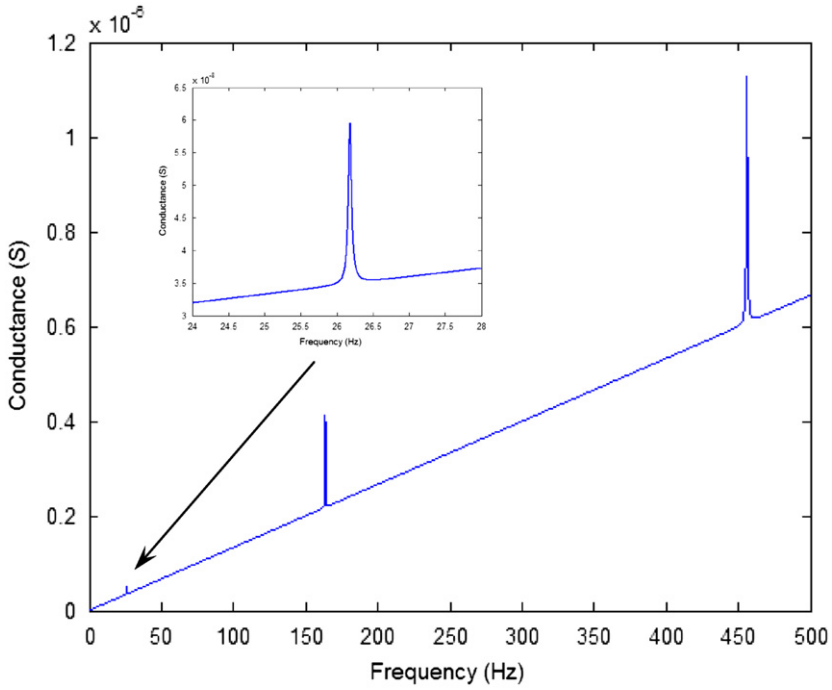

Fig. 4. Comparison study for a beam with one crack.

Table 2
Comparison study for a beam with one crack.

Natural frequency (Hz)	Ref. [10]	Ref. [34]	Present model
Mode 1	26.1015	26.1231	26.19
Mode 2	163.5959	164.0921	163.60
Mode 3	456.3634	459.6028	455.84

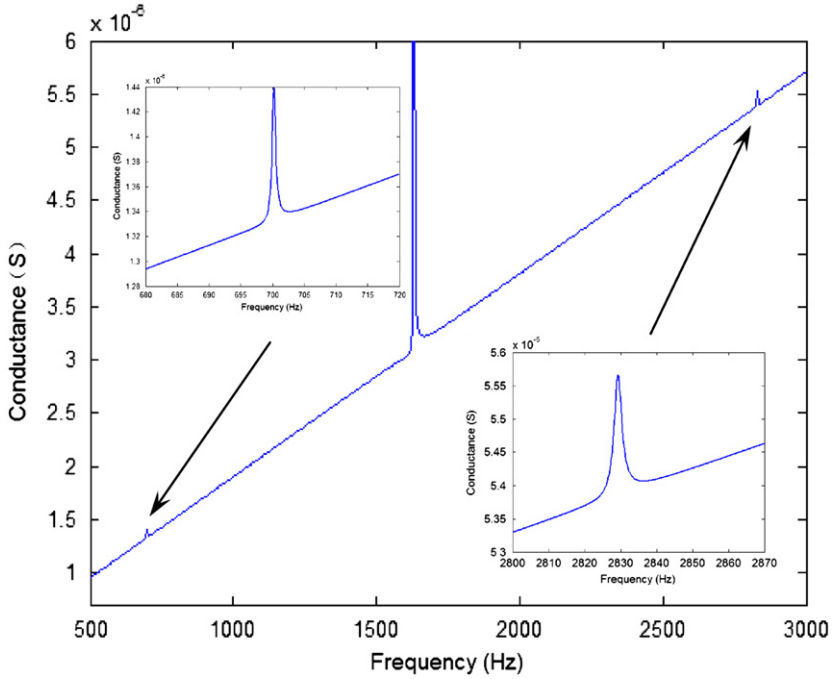

Fig. 5. Calculated results for a single beam with a crack for comparison with the experiment in Ref. [35].

Table 3
Material constants of the composite beam [8–11].

E_m (GPa)	E_f (GPa)	G_m (GPa)	G_f (GPa)	v_m	v_f	ρ_m (kg/m^3)	ρ_f (kg/m^3)
2.756	275.6	1.036	114.8	0.33	0.2	1600	1900

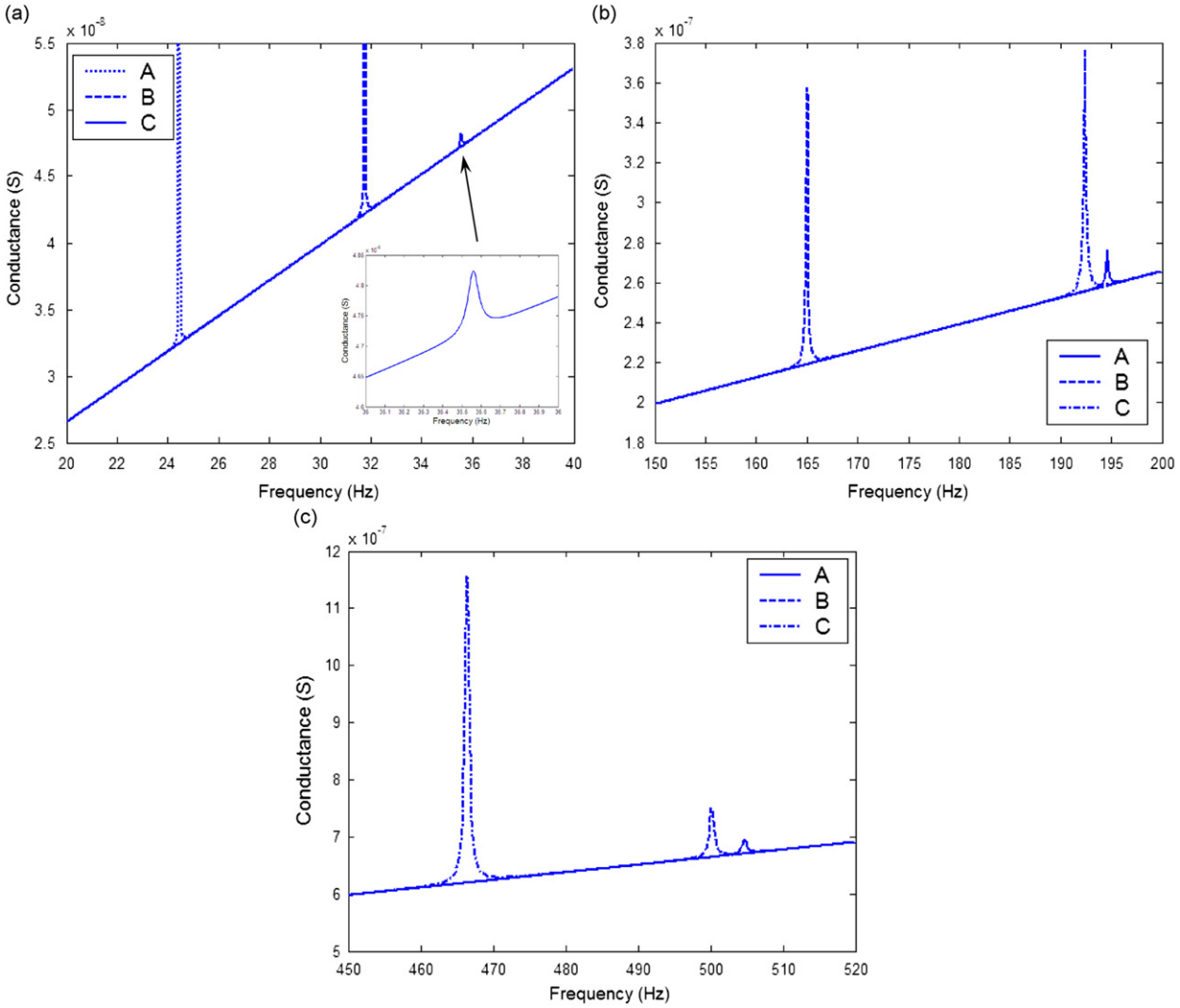

Fig. 6. Comparison study for a composite beam with three cracks. (a) First mode, (b) second mode and (c) third mode.

Table 4
Comparison study for a composite beam with three cracks.

Crack locations	Natural frequency (Hz)	Ref. [10]	Present model	Percentage difference (%)
A	Mode 1	22.362	24.42	8.43
	Mode 2	189.486	194.6	2.63
	Mode 3	495.819	504.6	1.74
B	Mode 1	30.637	31.68	3.29
	Mode 2	157.036	164.9	4.77
	Mode 3	484.878	500.1	3.04
C	Mode 1	35.629	35.57	−0.17
	Mode 2	186.156	192.4	3.25
	Mode 3	451.721	466.2	3.11

and the fixed end. For example, (0.1; 0.2; 0.3) and (0.5) denote three cracks located at 0.1, 0.2 and 0.3 m and a single crack located at 0.5 m from the clamped end of the beam, respectively.

4.2. Effect of the bond layer

Eqs. (2) and (8) have shown us the viscoelastic properties of the bond layer. For the sake of convenience in the following discussion, the shear stiffness of bond layer is always assumed to be 1 GPa [25]. Unless otherwise stated, the volume

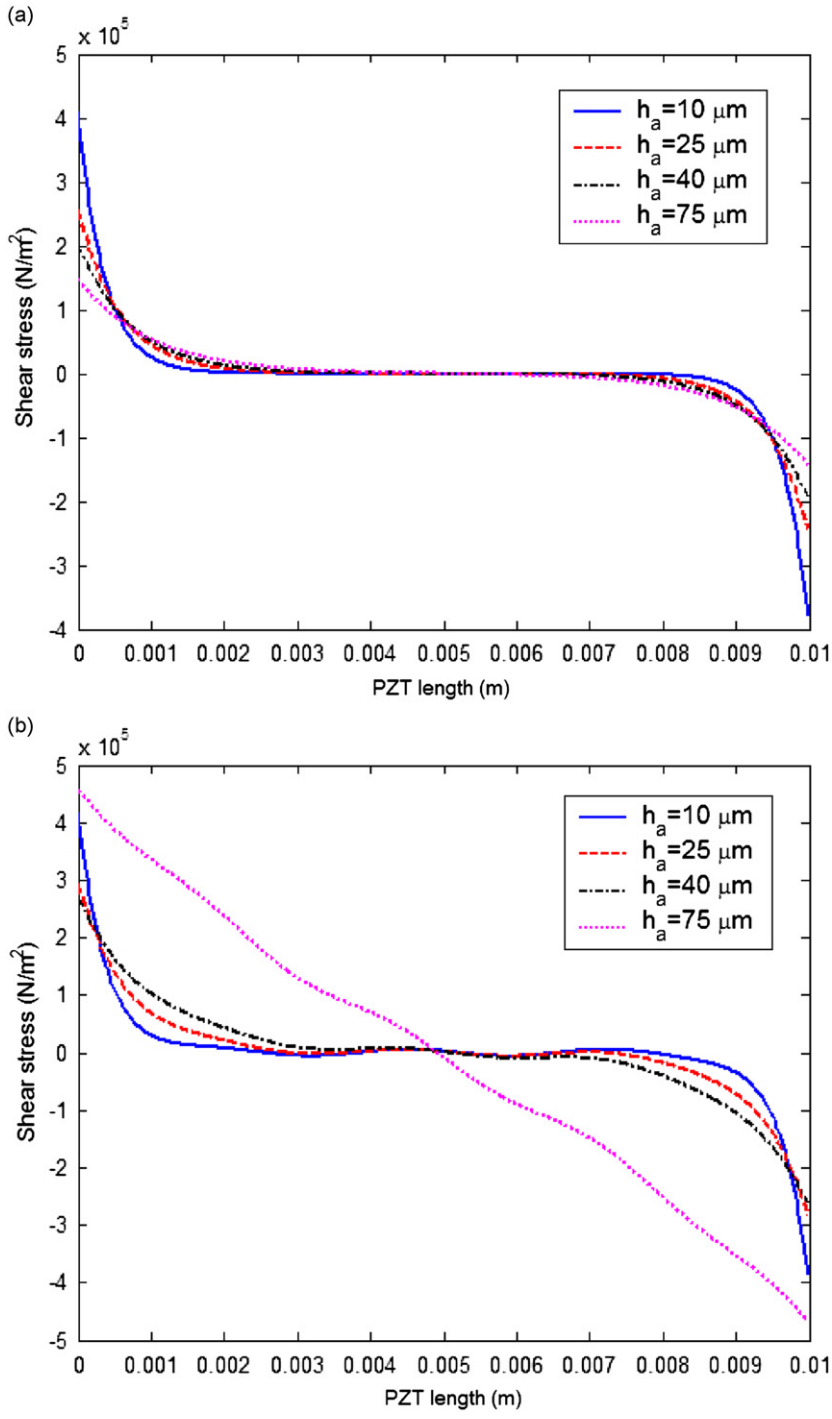

Fig. 7. Shear stress along PZT patch for various bonding layer thicknesses. (a) c_b=0, f=10 kHz and (b) c_b=0, f=450 kHz.

fraction of fibres V and the angle of the fibre θ are always assumed to be 0.5 and 45°, respectively. A pair of PZT patches symmetrically bonded onto the beam is located at 0.15 m from the fixed end.

Fig. 7 shows the shear stress distribution along the PZT patch for the cases where f=10 and 450 kHz and for various bond layer thicknesses 10, 25, 40, 75 μm. The effect of viscosity is ignored here. For a thinner bond layer, the shear stress becomes more confined to the PZT wafer ends. This agrees well with that observed by Giurgiutiu [19] under the quasi-static condition. For a relatively higher frequency electric excitation with f=450 kHz, however, the distribution of shear stress becomes more complicated as shown in Fig. 7(b). The distribution curves of shear stress between PZT patches and host beam under various excitation frequencies are also given in Fig. 8. It is shown that forcing frequency has a significant influence on the shear stress distribution and a sinusoidal distribution curve appears for a higher frequency electric excitation instead of the relatively simple curves for the lower modes. The similar phenomenon has been reported in Ref. [37]. It actually confirms the significance of the inertia effect of piezoelectric actuators.

As another parameter influencing the mechanical properties of the bond layer, the coefficient of viscosity c_b is taken from 10 to 10 000 Pa s in the simulation to investigate its effect on the stress transfer between the PZT patches and the host beam. In this case, c_b=10 Pa s represents very weak viscosity and c_b=10 000 Pa s represents very strong viscosity [25]. From Fig. 9, we can see that the shear stress distribution along the actuator/sensors changes slightly under a relatively lower frequency electric excitation with f=10 kHz, and however it becomes more complicated at a higher frequency with f=200 kHz, especially for the stronger viscosity with $c_b > 1000$ Pa s.

4.3. *Effect of various physical parameters on EMI signatures*

The effects of some physical parameters such as the volume fraction and the ply-angle of the fibres on the first several natural frequencies have been well investigated in the past decades [8–11]. However, the focus of this work is on the study of the effect of the various physical parameters on EMI signatures in the higher frequency range. To understand the effect of adhesive properties on the electro-mechanical impedance signatures, different values of viscosity and thicknesses of the bond layer are now assumed. When the viscosity of the adhesive becomes stronger (i.e. the coefficient of viscosity c_b increases), the curve of conductance subsides down clearly, especially for the stronger viscosity with $c_b > 1000$ Pa s. However, it is interesting to note that no peak shift of conductance curve occurs as shown in Fig. 10. This is mostly due to the fact that the viscosity of the adhesive does not change significantly the global stiffness of structure although a coupled model is considered here. Although the curve of conductance changes more slightly, the similar trend can also be observed from Fig. 11 for the parameter study with different thicknesses of the bond layer. This agrees well with that observed by Bhalla and Soh [20] and Yan et al. [31].

Because the increasing of the ply-angle is accompanied by a great decrease of natural frequencies, we can see from Fig. 12 that the resonant peaks of the conductance curve shift towards the left significantly with increasing ply-angle due

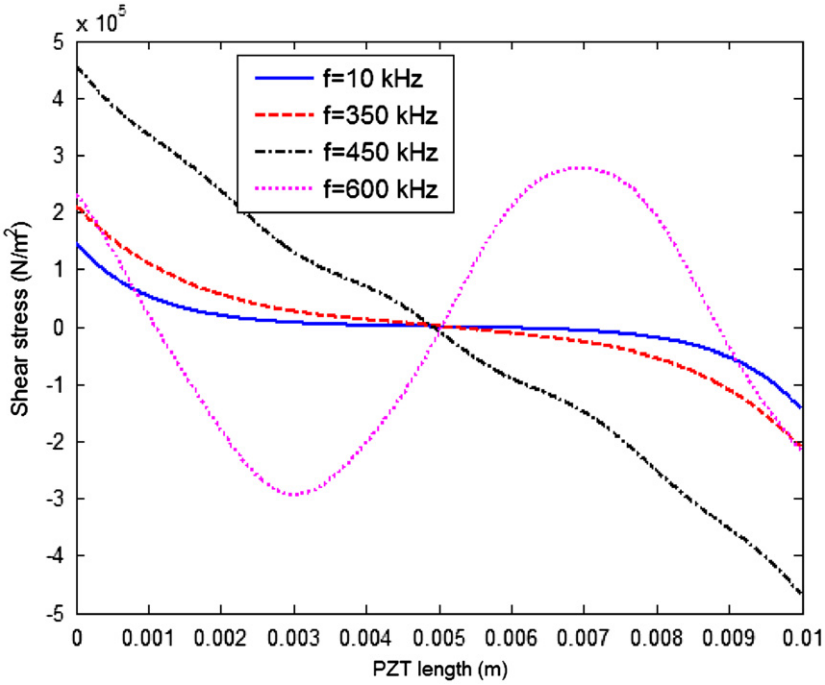

Fig. 8. Shear stress along PZT patch under different frequencies excitation (c_b=10 Pa s, h_b=75 μm).

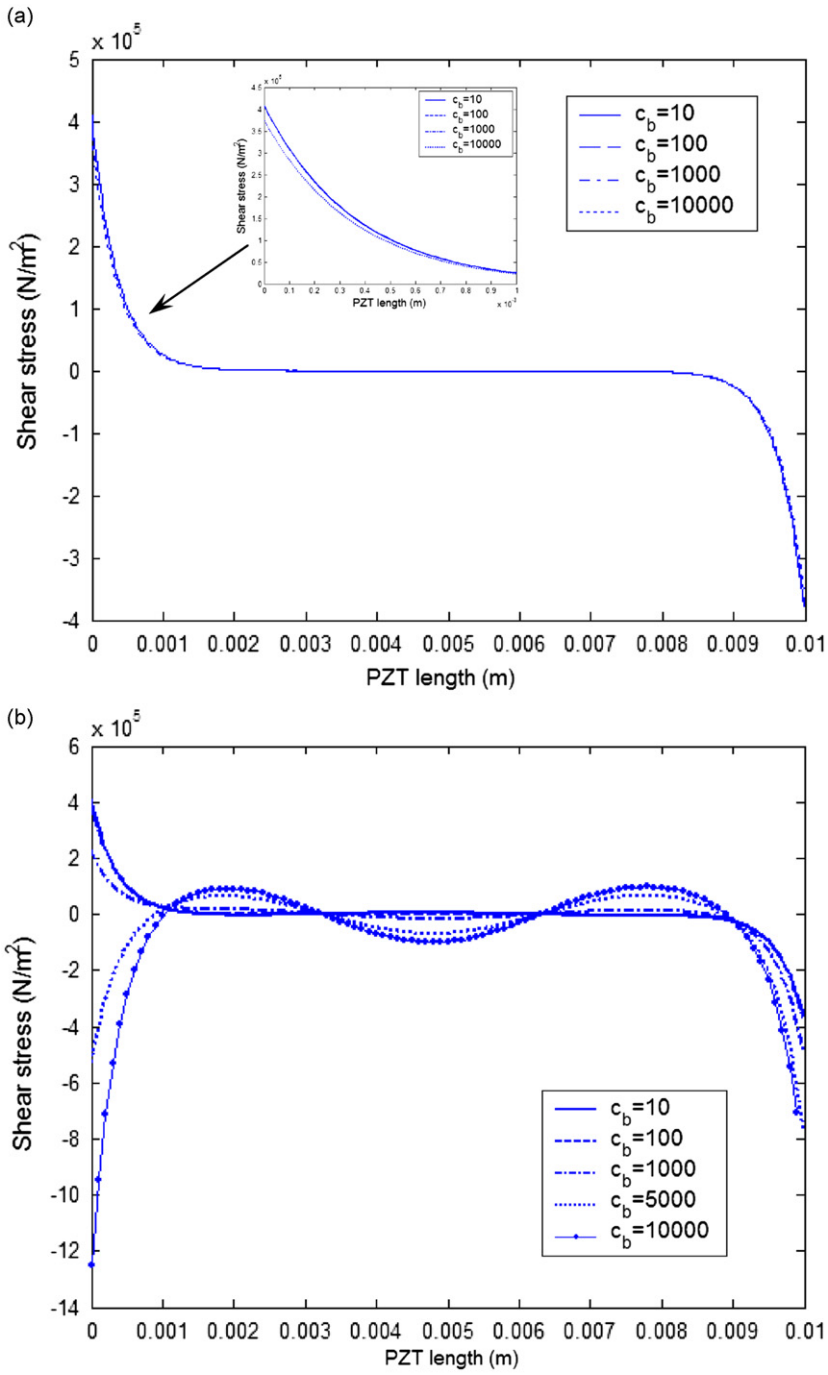

Fig. 9. Shear stress along PZT patch for various viscosity values of the bonding layer. (a) h_b=10 μm, f=10 kHz and (b) h_b=10 μm, f=200 kHz.

to reduction of the global stiffness of the host beam. However, a slight shift of the resonant peaks can be observed for larger ply-angles from 80° to 86° as shown in Fig. 13. This indicates that the stiffness of the composite beam is insensitive to the change of the ply-angle close to 90°. The similar phenomena have been observed for non-cracked or cracked composite beam at the first three natural frequencies [10,11].

The effect of volume fraction of the fibres V on EMI signatures is also investigated as plotted in Fig. 14. The conductance curves change dramatically with the increasing volume fraction of fibres from 0 to 0.7 and it seems that no more information about the composite can be found from Fig. 14. The further investigation shows that the resonant peaks of the conductance curve shift towards the right clearly with the increasing volume fraction of fibres from 0.50 to 0.53

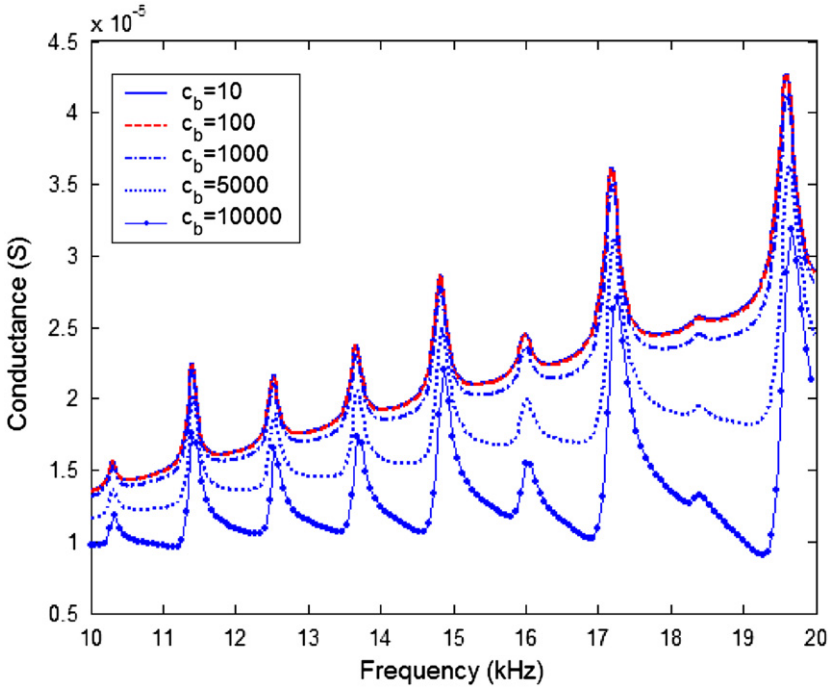

Fig. 10. EM admittance signatures for various viscosity values of the bonding layer (h_b=10 μm).

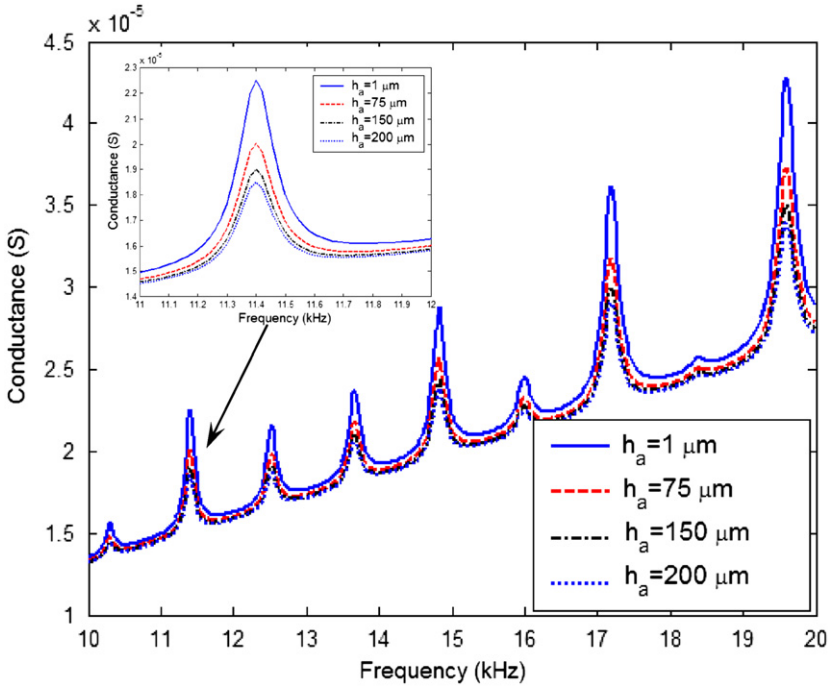

Fig. 11. EM admittance signatures for various bonding layer thicknesses (c_b=0).

(see Fig. 15). This indicates that the increasing of the volume fraction of fibres is accompanied by a significant increase in structural stiffness. It can also be observed from Eqs. (5), (6) and (A.3) (in Appendix A) that the transverse bending stiffness S_{11} will increase significantly with the increasing volume fraction of fibres V for the case of $E_f \gg E_m$ adopted here.

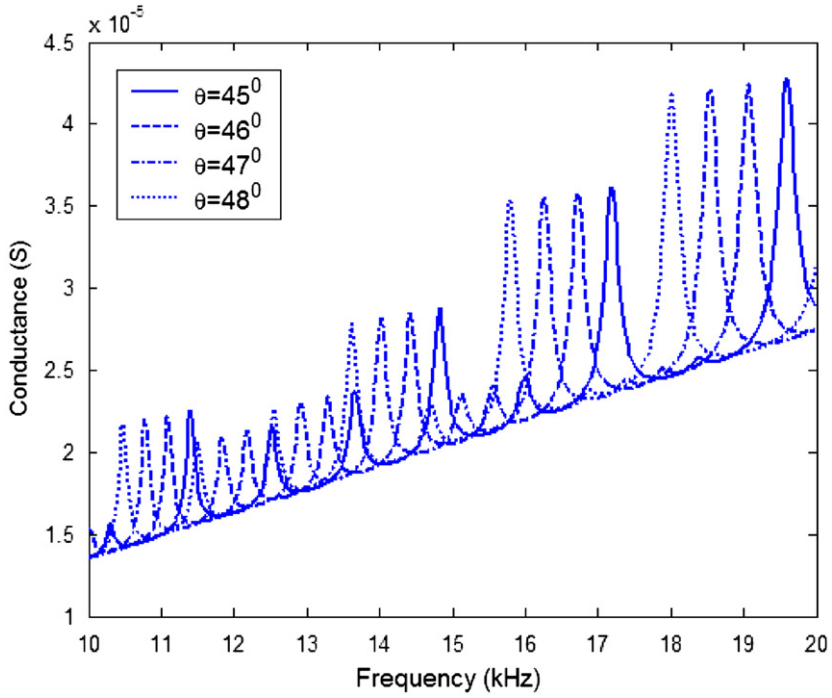

Fig. 12. EM admittance signatures for various ply-angles (θ=45–48°).

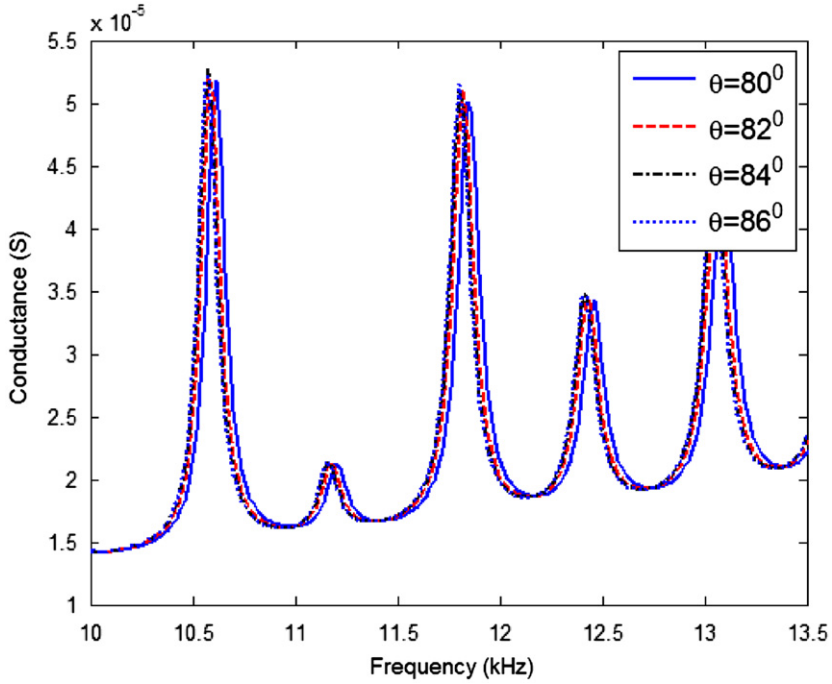

Fig. 13. EM admittance signatures for various ply-angles (θ=80–86°).

4.4. Crack detection based on EMI method

Based on the electric conductance spectra, the present model is now employed to quantitatively identify cracks due to changes in structural stiffness. Three common crack growth cases are considered in this paper: (1) progressive crack depth from 5 to 15 mm at the same location 0.3 m from the fixed end; (2) a single crack with depth 10 mm located at 0.1, 0.2 and

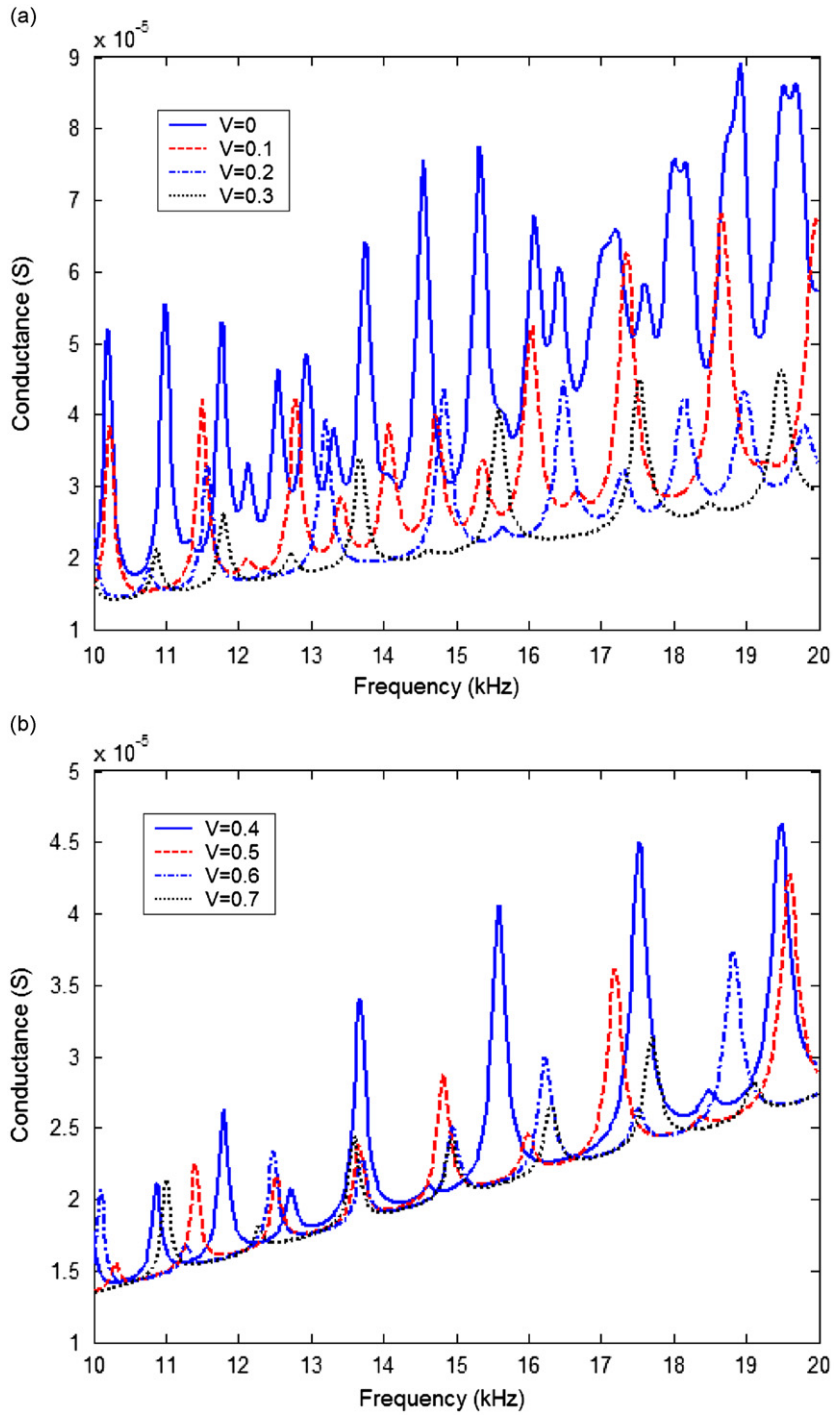

Fig. 14. EM admittance signatures for various volume fractions of fibres (V=0–0.7).

0.3 m, respectively, from the fixed end; (3) crack propagation through the composite beam. Fig. 16 shows that the EMI signatures are very sensitive to damages and the resonant peaks of the EMI signatures shift towards the left with increasing crack depth due to the reduction of global stiffness of the composite beam. The great effect of crack locations on the EMI signatures is also shown in Fig. 17. However, a slight shift of the resonant peaks of the EMI signatures can be observed for the same crack growth cases when the ply-angle of the fibre becomes 90°, as shown in Figs. 18 and 19, respectively. The numerical results consequently reveal that, corresponding to the ply-angle θ=90°, the resonant

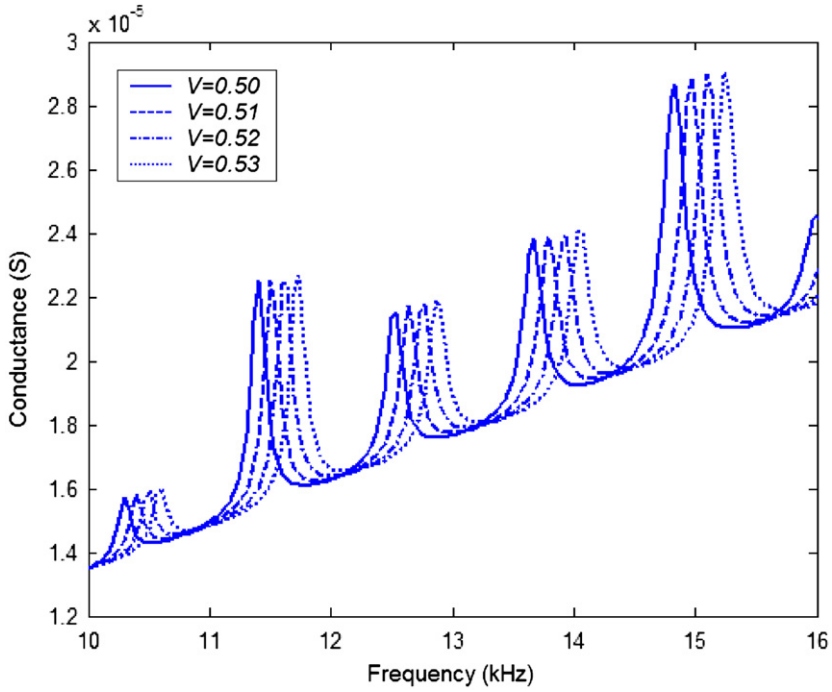

Fig. 15. EM admittance signatures for various volume fractions of fibres (V=0.5–0.53).

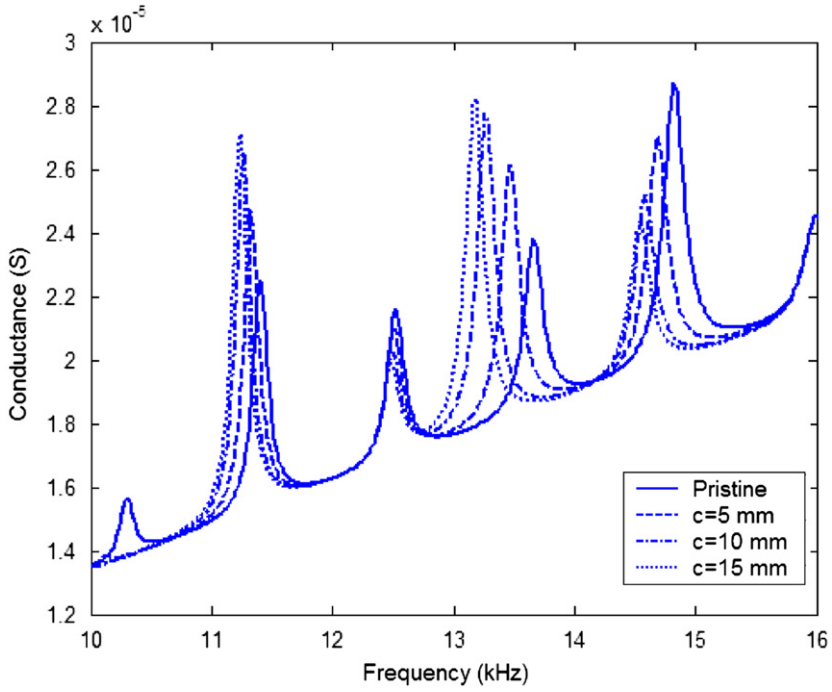

Fig. 16. EM admittance signatures for various crack depths (θ=45°).

frequencies are insensitive to the variation of the crack depth and crack location. This agrees well with that observed by Song et al. [10] at low frequencies. It should be pointed out that the ply-angle α defined in Ref. [10] is considered to be positive when measured from the positive y-axis in the counterclockwise direction and thus we have θ=90° in the case of α=0°.

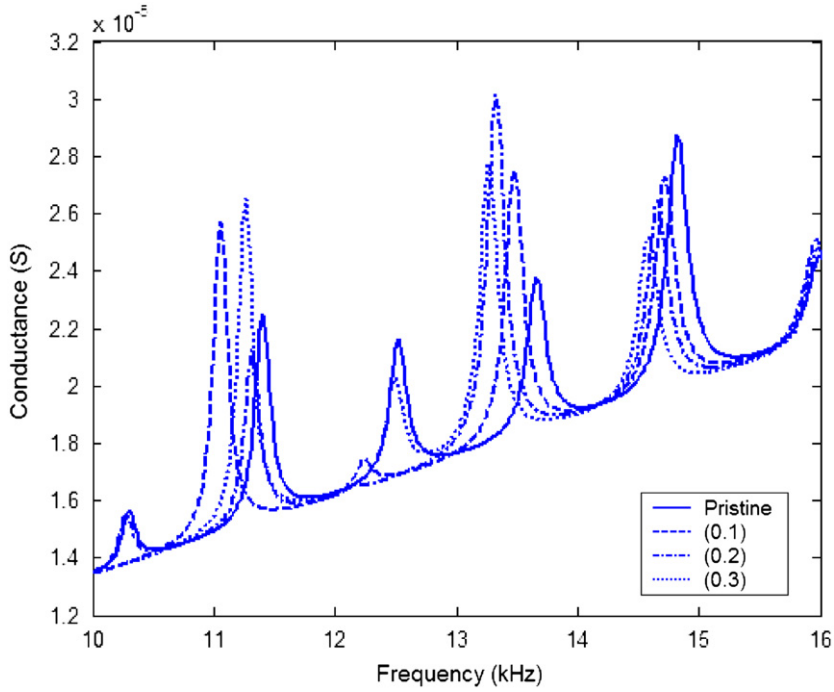

Fig. 17. EM admittance signatures for various crack locations (θ=45°).

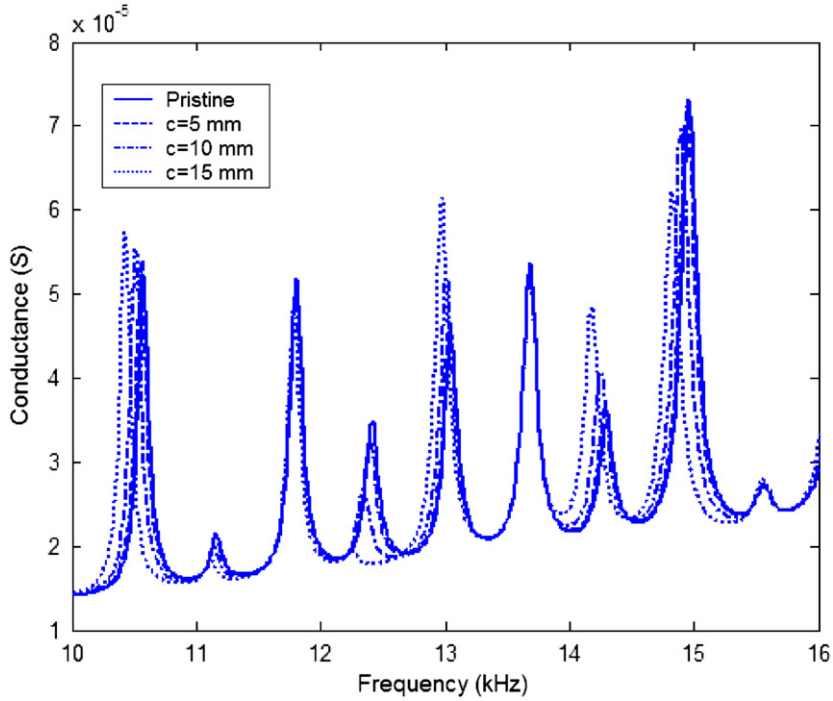

Fig. 18. EM admittance signatures for various crack depths (θ=90°).

To model crack propagation in the following case, we assume that the crack with depth 5 mm is located at 0.3 m from the beam root first, followed by simultaneous cracks located at 0.3 and 0.5 m, and finally simultaneous cracks located at 0.3, 0.5 and 0.6 m from the fixed end. We can see from Fig. 20 that the resonant peaks shift towards the left clearly with the crack propagations due to reduction of global stiffness of the host beam.

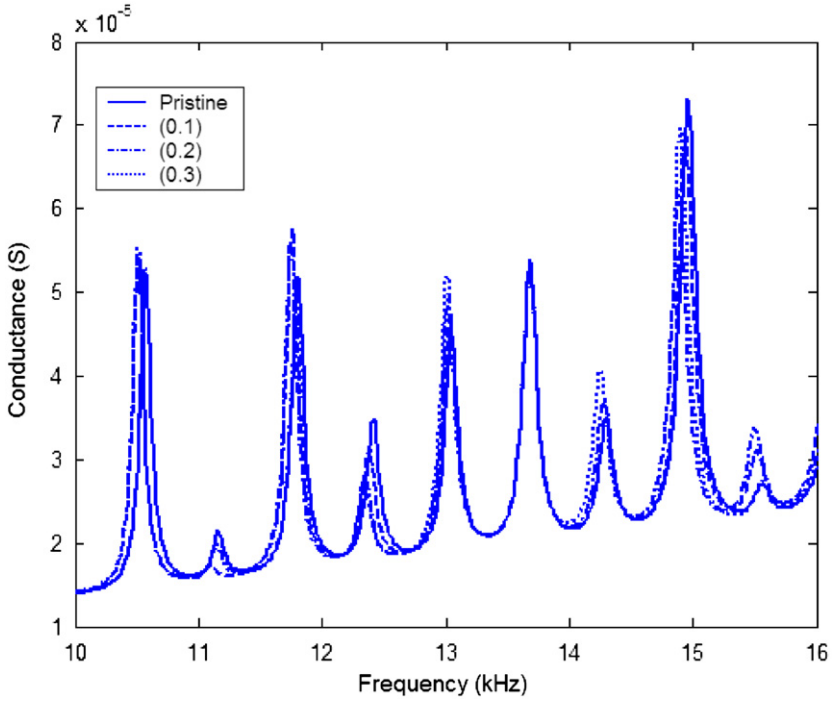

Fig. 19. EM admittance signatures for various crack locations (θ=90°).

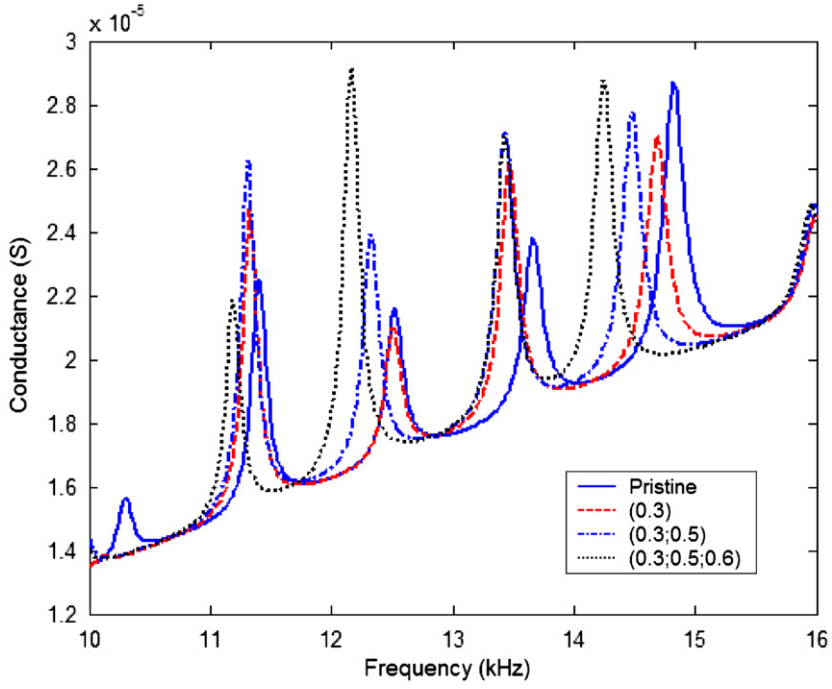

Fig. 20. EM admittance signatures for crack propagation (θ=45°).

By investigating the above numerical examples, we can make a conclusion that the technology developed in this paper is able to provide us an effective way to detect crack depth, location and propagation in a composite beam. However, it should be noted that the EMI signatures may be insensitive to the cracks appearing in the composite beams under some special conditions such as for the case of ply-angle θ=90°.

5. Conclusions

In this paper, an analytical technology relating the EMI signatures in the high-frequency range to dynamics of an anisotropic composite beam with multiple cracks is presented. A viscoelastic model is adopted to investigate the behavior of bond layer between PZT patches and the host beam. Considering one-dimensional motion of the PZT wafers excited by the applied high-frequency alternating electric field, a coupled structural system consisting of PZT patch, bond layer and host beam is established and an analytical expression of electric admittance is then developed to quantitatively detect cracks in the composite beam based on MRRM.

A comparison with the existent numerical results validates the accuracy and effectiveness of the present formulations. The further parametric study indicates that some parameters such as the adhesive thickness, excitation frequency and the coefficient of viscosity affect remarkably the shear stress distribution between PZT wafers and host beam, especially in the high-frequency range. The effect of interfacial bonding behavior on EMI signatures is also investigated. With increasing viscosity and thickness of the adhesive, the impedance signature changes accordingly which is, however, quite different from the peak deviation of conductance spectra induced by cracks. This implies that even if the PZT patches are imperfectly bonded onto the host structure in practice, the EMI signature thus obtained may be still be valid and valuable for damage diagnosis through a proper analysis. Furthermore, the high-frequency EMI signatures are very sensitive to cracks appearing in the composite beams and the present model can also correlate changes in signatures to physical parameters of the host beam and hence provide further information on depth and propagation of the cracks. Thus, the proposed model provides an efficient tool for analyzing high-frequency dynamic response of coupled structural system and also presents an effective and convenient method to identify the depth, location and propagation of cracks in the composite structures.

Acknowledgements

The work was sponsored by the National Natural Science Foundation of China (Grant nos. 50778161, 10725210), the National Basic Research Program of China (No. 2009CB623204), the Zhejiang Provincial Natural Science Foundation of China (No. Y107796), the Ningbo Natural Science Foundation of China (No. 2009A610148) and K.C. Wong Magna Fund in Ningbo University.

Appendix A

The compliance constants $\overline{b}_{ij}$ of the composite along the axes $x0y$ can be determined as follows [8,9,11]:

$$\begin{aligned}
\overline{b}_{11} &= b_{11}m^4+(2b_{12}+b_{66})m^2n^2+b_{22}n^4,\\
\overline{b}_{22} &= b_{11}n^4+(2b_{12}+b_{66})m^2n^2+b_{22}m^4,\\
\overline{b}_{12} &= b_{12}m^4+(b_{11}+b_{22}-b_{66})m^2n^2+b_{12}n^4,\\
\overline{b}_{16} &= (-2b_{11}+2b_{12}+b_{66})m^3n+(2b_{22}-2b_{12}-b_{66})mn^3,\\
\overline{b}_{26} &= (-2b_{11}+2b_{12}+b_{66})n^3m+(b_{22}-2b_{12}-b_{66})nm^3,\\
\overline{b}_{66} &= b_{66}m^4+2(2b_{11}-4b_{12}+2b_{22}-b_{66})m^2n^2+b_{66}n^4,
\end{aligned} \tag{A.1}$$

in which b_{ij} are compliance constants of the composite along the principle axes x_10y_1. b_{ij} are related to the mechanical constants of the materials by

$$\begin{gathered}
b_{11}=\frac{1}{E_{11}}\left(1-v_{12}^2\frac{E_{22}}{E_{11}}\right),\quad b_{22}=\frac{1}{E_{22}}(1-v_{23}^2),\quad b_{12}=\frac{-v_{12}}{E_{11}}(1+v_{23}),\\
b_{66}=1/G_{12},\quad b_{44}=1/G_{23},\quad b_{55}=b_{66},
\end{gathered} \tag{A.2}$$

where all elastic constants as well as the mass density ρ are calculated using the following formulations [8,9,11]:

$$\begin{gathered}
E_{11}=E_fV+E_m(1-V),\quad E_{22}=E_m\left[\frac{E_f+E_m+(E_f-E_m)V}{E_f+E_m-(E_f-E_m)V}\right],\\
v_{12}=v_fV+v_m(1-V),\quad v_{23}=v_fV+v_m(1-V)\left[\frac{1+v_m-v_{12}E_m/E_{11}}{1-v_m^2+v_{12}v_mE_m/E_{11}}\right],\\
G_{12}=G_m\left[\frac{G_f+G_m+(G_f-G_m)V}{G_f+G_m-(G_f-G_m)V}\right],\quad G_{23}=\frac{E_{22}}{2(1+v_{23})},\quad \rho=\rho_fV+\rho_m(1-V),
\end{gathered} \tag{A.3}$$

where subscript m and f denote matrix and fibre, respectively. E, G and v are the modulus of elasticity, the modulus of shear rigidity and Poisson's ratio, respectively. V is the volume fraction of fibres.

References

[1] B. Whittingham, H.C.H. Li, I. Herszberg, W.K. Chiu, Disbond detection in adhesively bonded composite structures using vibration signatures, *Composites and Structures* 75 (2006) 351–363.

[2] J. Pohl, S. Herold, G. Mook, F. Michel, Damage detection in smart CFRP composites using impedance spectroscopy, *Smart Materials and Structures* 10 (2001) 834–842.
[3] Z. Su, L. Ye, Quantitative damage prediction for composite laminates based on wave propagation and artificial neural networks, *Structural Health Monitoring* 4 (1) (2005) 57–66.
[4] P. Tan, L. Tong, Identification of delamination in a composite beam using integrated piezoelectric sensor/actuator layer, *Composites and Structures* 66 (2004) 391–398.
[5] Z. Wei, L.H. Yam, L. Cheng, Delamination assessment of multilayer composite plates using model-based neural networks, *Journal of Vibration and Control* 11 (2005) 607–625.
[6] C. Bois, P. Herzog, C. Hochard, Monitoring a delamination in a laminated composite beam using in-situ measurements and parametric identification, *Journal of Sound and Vibration* 299 (2007) 786–805.
[7] N.A. Chrysochoidis, D.A. Saravanos, Generalized layerwise mechanics for the static and modal response of delaminated composite beams with active piezoelectric sensors, *International Journal of Solids and Structures* 44 (2007) 8751–8768.
[8] M. Krawczuk, W.M. Ostachowicz, Modelling and vibration analysis of a cantilever composite beam with a transverse open crack, *Journal of Sound and Vibration* 183 (1) (1995) 69–89.
[9] M. Krawczuk, W.M. Ostachowicz, A. Zak, Modal analysis of cracked, unidirectional composite beam, *Composites Part B* 28B (1997) 641–650.
[10] O. Song, T.W. Ha, L. Librescu, Dynamics of anisotropic composite cantilevers weakened by multiple transverse open cracks, *Engineering Fracture Mechanics* 70 (2003) 105–123.
[11] M. Kisa, Free vibration analysis of a cantilever composite beam with multiple cracks, *Composites Science and Technology* 64 (2004) 1391–1402.
[12] C.K. Soh, K.K.H. Tseng, S. Bhalla, A. Gupta, Performance of smart piezoceramic patches in health monitoring of a RC bridge, *Smart Materials and Structures* 9 (2000) 533–542.
[13] V. Giurgiutiu., A.N. Zagrai, Embedded self-sensing piezoelectric active sensors for on-line structural identification, *Journal of Vibration and Acoustics* 124 (2002) 116–125.
[14] G. Park, A.C. Rutherford, H. Sohn, C.R. Farrar, An outlier analysis framework for impedance-based structural health monitoring, *Journal of Sound and Vibration* 286 (2005) 229–250.
[15] V.G.M. Annamdas, C.K. Soh, Embedded piezoelectric ceramic transducers in sandwiched beams, *Smart Materials and Structures* 15 (2006) 538–549.
[16] Y.W. Yang, Y.H. Hu, Electromechanical impedance modeling of PZT transducer for health monitoring of cylindrical shell structures, *Smart Materials and Structures* 17 (2008) 1–11.
[17] W. Yan, J.B. Cai, W.Q. Chen, Monitoring interfacial defects in a composite beam using impedance signatures, *Journal of Sound and Vibration* 326 (2009) 340–352.
[18] W. Yan, W.Q. Chen, Structural health monitoring using high-frequency electromechanical impedance signatures. Advances in Civil Engineering, 2010, 2010: 429148.
[19] V. Giurgiutiu, Tuned lamb wave excitation and detection with piezoelectric wafer active sensors for structural health monitoring, *Journal of Intelligent Material Systems and Structures* 16 (2005) 291–305.
[20] S. Bhalla, C.K. Soh, Electromechanical impedance modeling for adhesively bonded piezo-transducers, *Journal of Intelligent Material Systems and Structures* 15 (2004) 955–972.
[21] G. Park, C.R. Farrar, F.L. Scalea, S. Coccia, Performance assessment and validation of piezoelectric active-sensors in structural health monitoring, *Smart Materials and Structures* 15 (6) (2006) 1673–1683.
[22] X.P. Qing, H.L. Chan, S.J. Beard, T.K. Ooi, S.A. Marotta, Effect of adhesive on the performance of piezoelectric elements used to monitor structural health, *International Journal of Adhesion and Adhesives* 26 (8) (2006) 622–628.
[23] W. Yan, C.W. Lim, W.Q. Chen, J.B. Cai, Modeling of EMI response of damaged Mindlin-Herrmann rod, *International Journal of Mechanical Sciences* 49 (2007) 1355–1365.
[24] E.F. Crawley, J.D. Lius, Use of piezoelectric actuators as elements of intelligent structures, *AIAA Journal* 25 (10) (1987) 1373–1385.
[25] L. Han, X.D. Wang, Y. Sun, The effect of bonding layer properties on the dynamic behaviour of surface-bonded piezoelectric sensors, *International Journal of Solids and Structures* 45 (2008) 5599–5612.
[26] H. Fan, G.F. Wang, Interaction between a screw dislocation and viscoelastic interfaces, *International Journal of Solids and Structures* 40 (2003) 763–776.
[27] X. Wang, E. Pan, Interaction between a screw dislocation and a viscoelastic piezoelectric bimaterial interface, *International Journal of Solids and Structures* 45 (2008) 245–257.
[28] E.C. Pestel, F.A. Leckie, *Matrix Methods in Elasto Mechanics*, McGraw-Hill, New York, 1963.
[29] Y.H. Pao, W.Q. Chen, X.Y. Su, The reverberation-ray matrix and transfer matrix analyses of unidirectional wave motion, *Wave Motion* 44 (2007) 419–438.
[30] Y.H. Pao, W.Q. Chen, Elastodynamic theory of framed structures and reverberation-ray matrix analysis, *Acta Mechanica* 204 (2009) 61–79.
[31] W. Yan, C.W. Lim, W.Q. Chen, J.B. Cai, A coupled approach for damage detection of framed structures using piezoelectric signature, *Journal of Sound and Vibration* 307 (2007) 802–817.
[32] Y.Q. Guo, W.Q. Chen, Dynamic analysis of space structures with multiple tuned mass dampers, *Engineering Structures* 29 (2007) 3390–3403.
[33] X.D. Wang, G.L. Huang, The coupled dynamic behavior of piezoelectric sensors bonded to elastic media, *Journal of Intelligent Material System and Structures* 17 (2006) 883–894.
[34] E.I. Shifrin, R. Ruotolo, Natural frequencies of a beam with an arbitrary number of cracks, *Journal of Sound and Vibration* 222 (3) (1999) 409–423.
[35] H.P. Lin, Direct and inverse methods on free vibration analysis of simply supported beams with a crack, *Engineering Structures* 26 (2004) 427–436.
[36] W. Yan, W.Q. Chen, J.B. Cai, C.W. Lim, Quantitative structural damage detection using high frequency piezoelectric signatures via the reverberation matrix method, *International Journal for Numerical Methods in Engineering* 71 (2007) 505–528.
[37] X.D. Wang, G.L. Huang, Wave propagation in electromechanical structures: induced by surface-bonded piezoelectric actuators, *Journal of Intelligent Material Systems and Structures* 12 (2001) 105–115.